Citation for final published version:

Geng, Yanquan, Yan, Yongda, Brousseau, Emmanuel Bruno Jean Paul , Yu, Bowen, Qu, Shengnan, Hu, Zhenjiang and Zhao, Xuesen 2016. Processing outcomes of the AFM probe-based machining approach with different feed directions. Precision Engineering 46 , pp. 288-300. 10.1016/j.precisioneng.2016.05.009

Publishers page: http://dx.doi.org/10.1016/j.precisioneng.2016.05.0...

Processing outcomes of the AFM probe-based machining approach with different feed directions

Yanquan Geng[1,2], Yongda Yan[1*], Emmanuel B. Brousseau[2], Bowen Yu[1], Shengnan Qu[1], Zhenjiang Hu[1], Xuesen Zhao[1]

[1] *Key Laboratory of Micro-systems and Micro-structures Manufacturing of Ministry of Education, Harbin Institute of Technology, Harbin, Heilongjiang 150001, P.R. China*

[2] *Cardiff School of Engineering, Cardiff University, Cardiff, UK*

[*] *Corresponding author. Tel.: +86-0451-86412924. Fax: +86-0451-86415244*

E-mail address: yanyongda@hit.edu.cn *(Y. D. Yan)*

Abstract

We present experimental and theoretical results to describe and explain processing outcomes when producing nanochannels that are a few times wider than the atomic force microscope (AFM) probe using an AFM. This is achieved when AFM tip-based machining is performed with reciprocating motion of the tip of the AFM probe. In this case, different feed directions with respect to the orientation of the AFM probe can be used. The machining outputs of interest are the chip formation process, obtained machined quality, and variation in the achieved channel depth. A three-sided pyramidal diamond probe was used under load-controlled conditions. Three feed directions were first investigated in detail. The direction parallel to and towards the probe cantilever, which is defined as "edge forward", was then chosen for further investigation because it resulted in the best chip formation, machining quality, and material removal efficiency. To accurately reveal the machining mechanisms, several feed directions with different included angles for the pure edge-forward direction were investigated. Upon analysis of the chips and the machined nanochannels, it was found that processing with included angles in the range 0°–30° led to high-quality channels and high material-removal efficiency. In this case, the cutting angles, such as the rake angle, clearance angle, and shear angle, have an important influence on the obtained results. In addition, a machining model was developed to explain the observed machined depth variation when scratching in different feed directions.

Keywords: Atomic force microscopy; tip-based machining; feed direction; three-sided pyramidal probe; chip formation; machined depth.

Nomenclature

F_{N}	Applied normal load (μN)
K_{N}	Normal spring constant (N/m)
$\varDelta$	Feed (nm)
V_{tip}	Velocity of the AFM tip (μm/s)
V_{stage}	Velocity of the high precision stage (μm/s)
ε	Attack angle (radian)
γ	Semi-angle of the cutting tool in the vertical plane of the main cutting edge for the edge-forward direction (radian)

ω	Angle of the cutting tool in the vertical plane of the main cutting edge for the sideface-forward direction (radian)
κ	Included angle (radian)
α_n	Normal rake angle (radian)
β_n	Normal friction angle (radian)
β	Friction angle (radian)
φ_n	Normal shear angle (radian)
i	Inclination angle (radian)
η_c	Chip velocity angle (radian)
I	Normal plane perpendicular to the cutting edge
λ	Included angle between horizontal plane and plane I (radian)
F_t, F_r, F_a	Tangential, radial, and axial cutting forces (μN)
F_x, F_y, F_z	Cutting forces in the feed, friction, and normal directions (μN)
K_{tc}, K_{rc}, K_{ac}	Cutting coefficients in the tangential, radial, and axial directions (N/mm^2)
K_{te}, K_{re}, K_{ae}	Edge coefficients in the tangential, radial, and axial directions (N/mm)
r_e	Edge radius of the AFM tip (nm)
α_t	Effective rake angle (radian)
σ	Yield stress (MPa)
τ	Shear flow stress (MPa)
τ_1	Shear yield strength of the sample material along the sticking region (MPa)

p_0	Normal pressure at the AFM tip (N)
ρ	Distribution exponent
μ	Sliding friction coefficient for the tip–sample combination
Δ_c	Uncut chip thickness (nm)
V_f	Lateral signal of the photodetector of the AFM (V)
f	Sliding friction force of the tip–sample combination (μN)
α	Conversion factor between V_f and f (μN/V)
θ_0	Neutral point angle (radian)
θ_f	Front angle of the AFM tip (radian)
θ_b	Back angle of the AFM tip (radian)
θ_s	Side angle of the AFM tip (radian)
L_S	Tip setback value (μm)
H	Height of the AFM tip (μm)
h_e	Experimental machined depth (nm)
h_t	Theoretical depth calculated from the developed model (nm)
s	Number of cutting lines generated by reciprocating motion of the AFM tip

1. Introduction

Recent developments in nanotechnology-based applications have driven demand for high-quality nanochannels with accurate and repeatable dimensions for application in various fields, such as in nanofluidics [1,2], nanosensors [3,4], and nanoelectronics

[5,6]. However, fabricating such nanochannels poses several challenges [7]. Several resist- and vacuum-based patterning techniques exist to create nanoscale channels, such as electron-beam and extreme-ultraviolet lithography. However, the high capital investment and restricted set of substrate materials needed for these techniques have motivated the development of alternative and unconventional nanofabrication processes [8–10].

Since the invention of the atomic force microscope (AFM) by Binnig et al. in 1986, AFM probe-based fabrication has become a powerful and flexible method to manufacture nanoscale structures. This is because of the inherent capability of AFM instruments for atomic-level manipulation, their relatively low technological requirements and cost, and their ability to operate in the atmospheric environment [11,12]. Direct mechanical AFM probe-based machining has been widely used to fabricate one-dimensional nanofeatures [13,14], two-dimensional micro/nanostructures [12,15], and even three-dimensional micro/nanocavities [16,17]. When operating under load-controlled mode, this process can also be used to carry out high-quality machining on an inclined [18] or even curved surface [19].

An important engineering challenge that needs to be addressed when conducting AFM probe-based machining is to estimate the load that must be applied by the tip on the processed specimen to achieve a particular machined depth. Several methods have been proposed to reveal the relationship between the applied normal force and the machined depth. Tseng et al. [20] and Dong et al. [21] experimentally found that the increase of the depth and width of cut grooves with applied normal force follows a logarithmic law. Wang et al. [22] and Geng et al. [23] developed theoretical models to express the relationship between the applied normal force and the depth of channels machined using a multipass scratching method. Lin et al. [24] proposed a theory to calculate objective functions through step-by-step adjustments of the increased cutting depth. These theoretical studies focused on the machined depth created by scratching on the same groove several times. More recently, an experimental fit method [25] and a theoretical model [16] have been proposed to predict the machined depth when parallel grooves are cut along a feed direction to achieve width-controllable nanochannels or complex nanostructures. However, in these studies, the influence of the feed direction with respect to the orientation of the tip and the chip formation phenomenon were not considered. Further, the geometric shape of the probe was assumed to be conical with a spherical apex.

A recent study of the contact area between the AFM probe and the chips formed when cutting single grooves with different scratching directions indicated that the machining orientation has a large influence on obtained depth and quality because of the particular geometry of the three-sided pyramidal diamond AFM tip [26]. However, this study only focused on chip formation and the machined depth of single grooves. To fabricate more complex nanostructures, cutting cavities composed of a series of parallel and adjacent grooves along a feed direction is required. However, no previous studies have focused on the chip formation process and the influence of the cutting angles during nanoscratching of such cavities. Therefore, similar to traditional machining, the chip formation process and the cutting angles should be investigated in detail when scratching with different feed directions with respect to the orientation of the AFM probe to obtain predictable nanochannels or complex nanostructures.

In the present study, reciprocating motion of the AFM tip and displacement of the stage are combined to achieve nanochannels that are a few times wider than the AFM probe, using the AFM-based nanoscratching method on the surface of a processed specimen. To achieve this, three feed directions are first investigated and then further investigations are performed by incrementally varying the processing angle for a selected feed direction. Chip formation and the quality of the machined channels are analyzed for each condition. Finally, a theoretical model is developed that considers the cutting angles to explain the differences in the obtained machined depths when using different feed directions.

2. Experimental methodology

2.1 AFM probe-based machining setup

Fig. 1(a) shows a schematic diagram of the modified AFM nanomachining system used in this study, which includes a commercial AFM (Dimension 3100; Veeco Inc., USA) and two high precision stages (M511.HD; PI Company, Germany). These stages are used to control the relative movement between the sample and the AFM tip in the lateral *x* and *y* directions. They are driven by a motor and a piezoelectric transducer (PZT) with a high-resolution encoder as the measurement device. The displacement range and resolution for both axes are 100 mm and 2 nm, respectively. A diamond tip (PDNISP; Veeco Inc., USA) is used for all nanomachining operations. The cantilever on which the diamond tip is mounted is made of stainless steel and has a calibrated normal spring constant (K_N) of 275 N/m, as specified by the probe manufacturer. The radius of the tip is approximately 86 nm. This was determined using the blind tip reconstruction method [27]. The diamond tip used in this study is a three-sided pyramid and its position relative to the cantilever is specified in Fig. 1(b). In particular, the front angle (θ_f), back angle (θ_b), and side angle (θ_s), as defined in Fig. 1(c) and (d), are approximately 55°, 35°, and 51°, respectively. The height of the tip (H) and the tip setback value (L_S) are approximately 50 μm and 13 μm. These values were provided by the manufacturer.

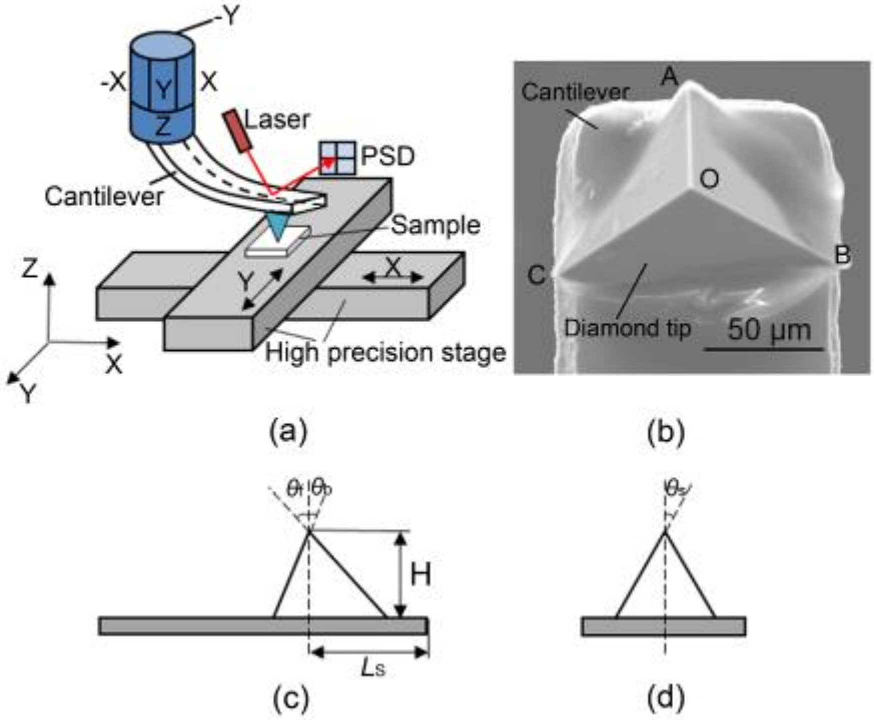

Fig. 1. (a) Schematic diagram of the modified AFM probe-based machining system, (b) image of the diamond probe, and schematic diagrams of (c) side and (d) front views of the diamond tip.

2.2 Planning the machining paths

Based on this modified AFM system, the procedure for conducting the machining operations is as follows:

(1) The AFM tip approaches the sample until the normal load value set by the user is reached. This results in the tip pressing into the surface of the sample. In conventional contact mode AFM scanning, the normal load can be kept constant by controlling the height of the PZT on which the probe is attached to keep the deflection of the cantilever constant. Similarly, during AFM probe-based machining, this normal load is used to control the depth of the generated nanostructures.

(2) The displacement of the PZT of the AFM in the slow-scanning direction is disabled so that the tip performs only a reciprocating motion. In this case, the high-precision stage is moved at a low velocity to carry out machining of nanochannels with different directions with respect to the probe. With this configuration, the width of the produced nanochannels is defined by the amplitude of the tip reciprocating motion while the movement of the stage determines their length.

(3) Once a nanochannel is machined, the AFM tip is lifted up and the high-precision stage moves the sample to a follow-up position where a subsequent nanochannel can be cut.

The sample used in this study was a 2A12 aluminum alloy with high surface quality obtained by single-point diamond turning. The surface roughness was approximately 5 nm. Both scanning electron microscopy (SEM) and an AFM were used to inspect the machined nanochannels. The sample was immediately analyzed after machining by SEM. An AFM was used to analyze the samples after they were ultrasonically cleaned in alcohol solution for about 10 min to remove chips formed during the machining process.

3. Results and discussion

3.1 Main feed directions with respect to the long axis of the probe cantilever

The typical relative directions of motions between the reciprocating displacement of the tip and continuous movement of the high-precision stage are shown in Fig. 2. Three feed directions were investigated. (1) Movement of the high-precision stage parallel and towards the probe cantilever (i.e., edge-forward in Fig. 2(a)). (2) Movement of the stage parallel and away from the probe cantilever (i.e., face-forward in Fig. 2(b)). In these two cases, the reciprocating motion of the tip was carried out perpendicular to the long axis of the probe cantilever. (3) Movement of the stage perpendicular to the cantilever (i.e., sideface-forward in Fig. 2(c)). In this case, the reciprocating motion of the tip was conducted along the long axis of the probe cantilever, as shown in Fig. 2(c).

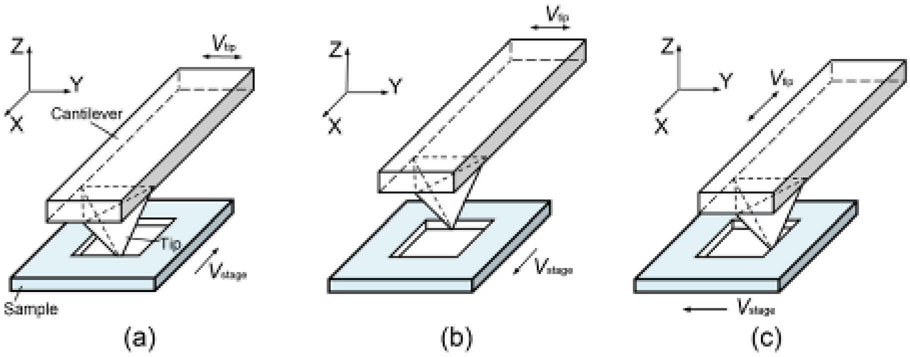

Fig. 2. Schematic diagrams of the three feed directions considered: (a) edge-forward, (b) face-forward, (c) sideface-forward.

Fig. 3 shows side- and cross-section views along a plane perpendicular to the cutting edge for the three feed directions. The distance travelled by the AFM tip on the sample along the direction of the stage motion in one reciprocating cycle is defined as the feed (Δ), as shown in Fig. 3. The normal load (F_N) can be calculated by

$$F_{\mathrm{N}} = \mathrm{setpoint} \times \mathrm{sensitivity} \times K_{\mathrm{N}} \quad (1)$$

The setpoint indicates the expected voltage value of laser reflection on the position sensitive detector (PSD), which can be set before machining. The sensitivity represents the relationship between the voltage of laser reflection on the PSD and deflection of the cantilever in the Z direction. Δ', x', and y' in Fig. 3(d), (e), and (f) are defined as the projections of the feed, x axis, and y axis in the considered cross-section, respectively. Figs. 4 and 5 show SEM and AFM images of the nanochannels machined with a feed of 120 nm and a set normal load of 67 μN in the three feed directions. The width of each nanochannel was 20 μm and the velocity of the tip (V_{tip}) was 80 μm/s. Fig. 4(a), (b), and (c) show SEM images of the complete channels, and Fig. 4(d), (e), and (f) show magnified SEM images of chips or burrs formed during the machining process.

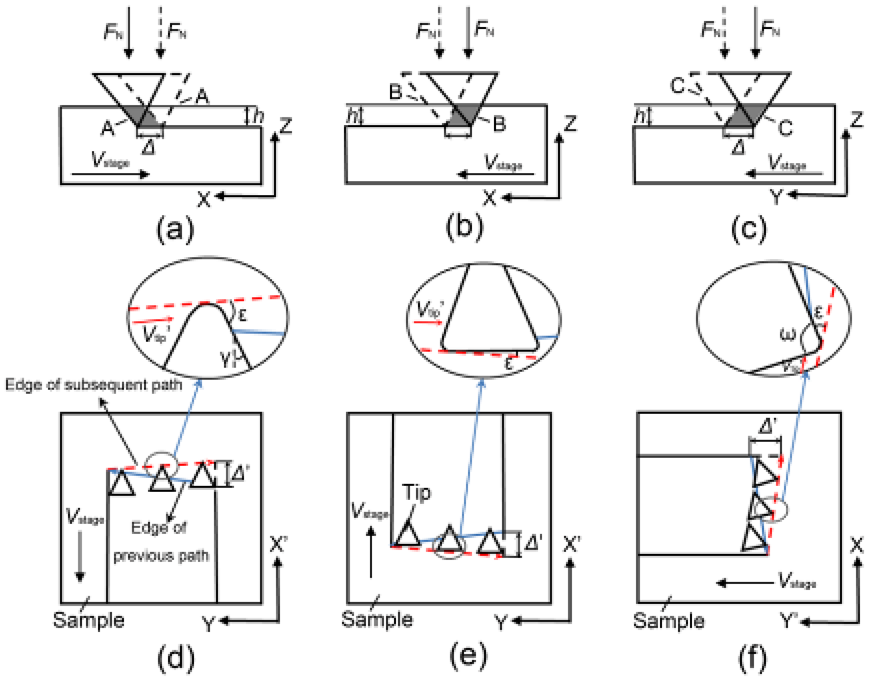

Fig. 3. Schematic diagrams of side views of the nanomachining processes: (a) edge-forward, (b) face-forward, and (c) sideface-forward. Schematic diagrams of cross-sectional views of the nanomachining processes: (d) A-A section in Fig. 3(a), (e) B-B section in Fig. 3(b), and (f) C-C section in Fig. 3(c).

As shown in Fig. 2(a), for the edge-forward direction, the AFM carries out reciprocating motion along the *y* axis while the high-precision stage moves in the negative *x*-axis direction. Fig. 3(a) shows the side view of the corresponding feed direction and Fig. 3(d) shows the corresponding A-A cross-section. In this case, the OA edge of the tip shown in Fig. 1(b) is the main cutting edge.

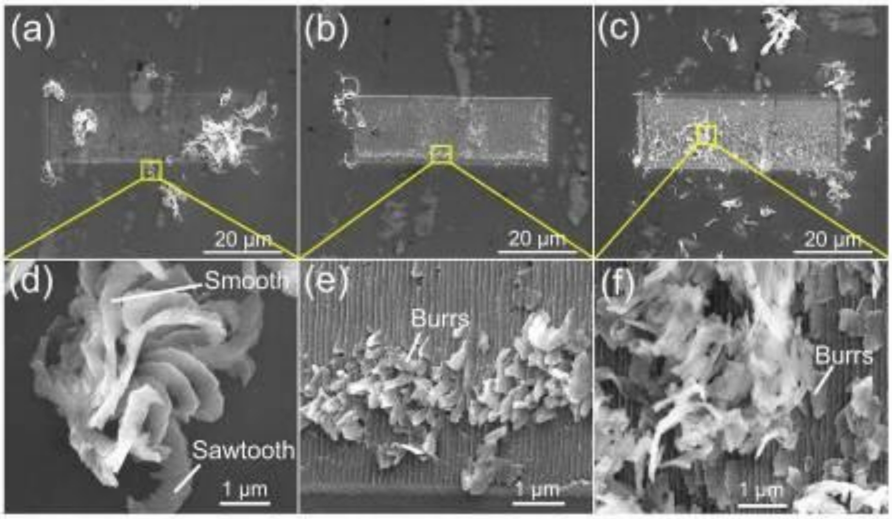

Fig. 4. SEM images of machined nanochannels: (a) edge-forward, (b) face-forward, and (c) sideface-forward. Magnified SEM images of chips or burrs: (d) edge-forward, (e) face-forward, and (f) sideface-forward.

As shown in Fig. 4(a), for the edge-forward machining condition, continuous chips formed without accumulating on the side of the nanochannel. As shown in the magnified SEM image of a typical chip in Fig. 4(d), one side of the chip has a sawtooth shape, whereas the other side is relatively smooth. The attack angle between the tip and the sample material ε (see Fig. 3(d)) can be used to determine the material removal mechanism. In particular, with increasing ε, three removal mechanisms have been proposed: plowing, wedge formation, and cutting [28].

For AFM-based diamond tip nanomachining of Si, it was reported that cutting is the dominant material removal phenomenon when $\varepsilon \geq 75°$ [29]. According to the specified geometry of the tip, the semi-angle of the cutting tool in the vertical plane of the main cutting edge γ was determined to be ~45°, as shown in Fig. 3(d). Additionally, given that the width of the machined channel is much larger than the feed in the A-A cross-section, movement of the tip is mainly along the *y* axis, as shown in Fig. 3(d). When the tip starts a new reciprocating cycle, owing to the relatively small uncut chip thickness and the influence of the edge radius of the tip, the attack angle is not high enough to lead to cutting with chip formation. Thus, plowing is the most likely mechanism between the tip and the sample in this case. Therefore, as the uncut chip thickness increases, ε is calculated to be around 45°. Although the material used in this study is different from that investigated in Ref. [29], $\varepsilon = 75°$ can be used to determine the inherent cutting phenomenon. In this case, because 45° is significantly less than 75°, it seems that both cutting and plowing occur when machining in the edge-forward direction. This hypothesis is supported by the morphology of the generated chips. Specifically, the sawtooth shape on one side of the chips may be the result of extrusion of processed material when the machining state is composed of a mixture of plowing and cutting [30]. Given that continuous chips are formed, cutting may also play an important role in the machining process.

The sawtooth shape on one side of the chips can cause the chips to break, which could explain why almost no chips remain on the side of the channel after cleaning, as shown in Fig. 5(a). From the cross-sectional topography recorded along the length of the machined channel (Fig. 5(a)), a relatively well-defined channel with a depth of approximately 208 nm was obtained using the edge-forward feed direction. This value represents the average of three depth measurements taken at three different locations in the machined cavity. Along the width of this particular channel, the uncut chip thickness should vary in one reciprocating cycle, as shown in Fig. 3(d). Specifically, when the tip starts to travel from one side of the channel, the uncut chip thickness is relatively small, which this should result in a large machined depth because of the influence of the force-controlled feedback loop of the AFM system. With the increase of the uncut chip thickness as the tip moves along the width of the nanochannel, the machined depth should decrease until the tip reaches the opposite side of the channel. The tip is then made to scratch in the opposite reciprocating motion, and a similar effect on the scratching depth should occur. However, this time the lowest and highest uncut chip thicknesses are located on the opposite sides of the channel compared with the preceding tip movement along the channel width. Thus, the lowest and highest values of the uncut chip thickness alternate between both sides of the channels because of the reciprocating motion of the tip. Consequently, the machined depth on both sides of the nanochannel should also alternate. This is referred to as a wedge-shape [25], and this is often observed when scratching with a relatively large feed. Compared with the feed value in Ref. [25], the feed value in this study is relatively small, which results in small depth variation. Consequently, the machined depths on both sides of the nanochannel are relatively homogeneous and are similar to the depth in the middle of the channel. Therefore, the machined depth shows little variation along the channel cross-section, as shown in Fig. 5(a).

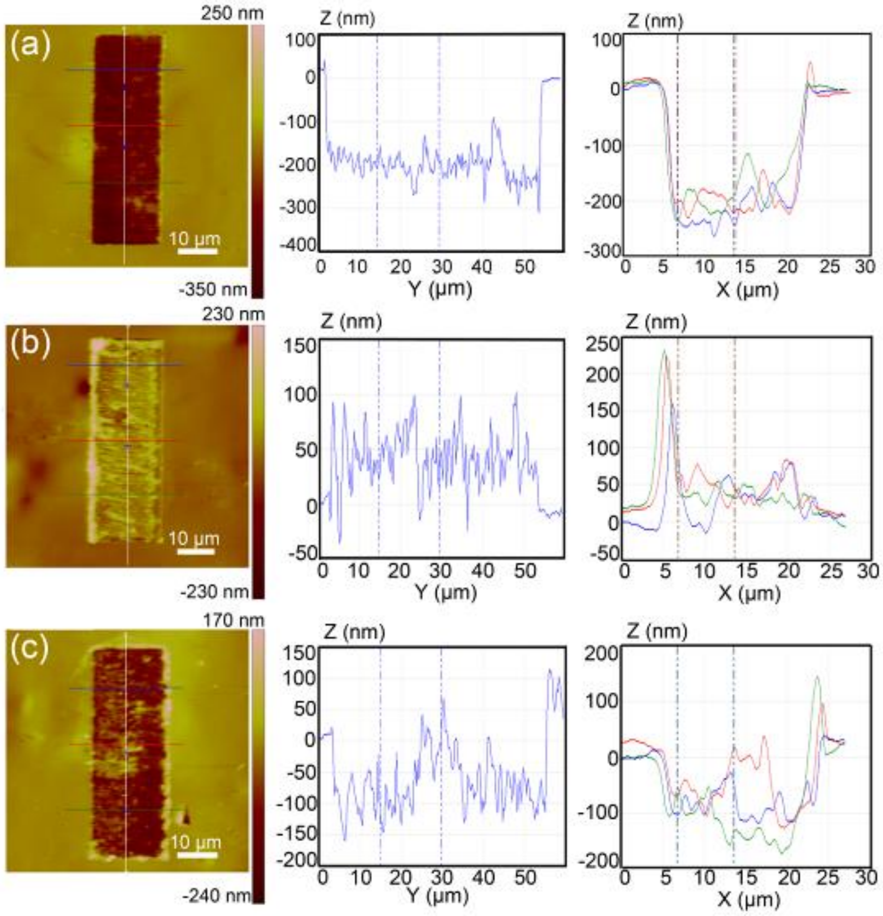

Fig. 5. AFM images of the machined nanochannels: (a) edge-forward, (b) face-forward, and (c) sideface-forward.

For the face-forward direction, the AFM carries out reciprocating motion along the *y* axis and the high precision stage moves in the positive *x*-axis direction, as shown in Fig. 2(b). Fig. 3(b) shows the side view of this nanomachining setup and Fig. 3(e) shows the B-B cross-section defined in Fig. 3(b). As shown in the magnified SEM image of burrs in Fig. 4(e), continuous chips were hardly generated with this cutting condition and burrs are very prominent on the sides of the produced grooves.

For the face-forward direction, from the AFM scan of the nanochannel obtained after cleaning (Fig. 5(b)), the channel does not have any depth along both the horizontal and longitudinal cross-sections. Possible reasons for this are the feed of scratching in the B-B cross-section (dozens of nanometers) being much smaller than the width of the machined channel (dozens of micrometers), and the attack angle of the main cutting edge being extremely small, as shown in Fig. 3(e). Moreover, two edges of the tip would participate in scratching: the main cutting edge mentioned above and an auxiliary cutting edge. Owing to the small machined depth and the relatively large radius of the tip, the function of the auxiliary cutting edge is not expected to be influential in this case. Thus, plowing is the dominant mechanism when the feed is in the face-forward direction and the material cannot be effectively removed. As a result, this feed direction is not suitable for the nanochannel fabrication process.

For the sideface-forward direction, the AFM is driven to carry out reciprocating motion along the x axis and the high precision stage is moving in the positive y-axis direction (Fig. 2(c)). In this case, the OC edge of the tip shown in Fig. 1(b) is the main cutting edge. Fig. 3(c) shows the side view of this nanomachining configuration and Fig. 3(f) shows the C-C cross-section perpendicular to the main cutting edge OC shown in Fig. 3(c). Based on the geometry of the tip, it is estimated that the angle ω shown in Fig. 3(f) is 90°. As shown in the magnified SEM image of typical chips and burrs (Fig. 4(f)), some chips formed using this feed direction and burrs were also generated. This is because the attack angle is ~26.5° along the positive x-axis direction when the tip is traveling along the width of the nanochannel, as shown in Fig. 3(f). This relatively small attack angle results in the plowing mechanism occurring, leading to formation of burrs. However, in the opposite reciprocating motion (i.e., along the negative *x*-axis direction), the attack angle and the clearance angle are estimated to be 63.5° and 26.5°, respectively. Although chips can form because of this relatively high attack angle, the clearance angle may not be sufficiently high to enable generation of continuous chips. Thus, only some intermittent chips are obtained with this feed direction. Moreover, from Fig. 3(f), two edges of the tip may participate in scratching with a relatively large feed at the end of the tip travelling trace. The main cutting edge is used to calculate the attack and clearance angles, which play the main role in surface formation and the quality of machined nanochannels. The auxiliary cutting edge will only participate in cutting when the cross-section of the tip is close to the bottom of the channel, which may lead to formation of some chips. Further, the three-sided pyramidal geometry of the tip would lead to the size of the cross-section increasing with increasing distance from the bottom of the channel. Thus, when the size of the cross-section of the tip reaches a certain value, the auxiliary cutting edge would not participate in cutting, even at the end of the tip travelling trace. In this study, the value of the feed is relatively small while the machined depth is greater than 100 nm. Thus, the effect of the auxiliary cutting edge on the machined outcomes is considered to be negligible. Considering the regular change in the material removal mechanism because of the alternate variation in the attack angle between two subsequent reciprocating motions, the machining process lacks stability. For this reason, there is large variation in the surface quality in the horizontal and longitudinal cross-sections of the nanochannel, as shown in Fig. 5(c). In light of the obtained machined quality, the sideface-forward feed direction is deemed unsuitable for fabricating nanochannels with the current setup. Further, as shown in Fig. 5(c), the depth of the nanochannel obtained in this case is approximately 100–150 nm, which is much smaller than that achieved in the edge-forward feed direction. Thus, the cutting angles that are inherent to the combination of the tip geometry and feed direction have a large influence on the process outcome, especially on the machined depth and surface quality at the bottom of nanochannels. The specific relationship between the cutting angle and the machined depth will be described in Section 3.3.

3.2 Variation of the angle between the feed direction and the tip reciprocating motion in the edge-forward configuration

Based on the above results, the edge-forward direction is the best feed direction among the three machining setups. However, given that $\varepsilon \approx 45°$, both the plowing and cutting mechanisms may occur during machining, and thus material removal may not be most effective in the "pure" edge-forward feed direction. Thus, in this section, cutting results obtained for different angles from the edge-forward direction are presented.

As shown in Fig. 6, the tip can be controlled to perform reciprocating motion at a certain orientation angle with respect to the main axis of the probe cantilever while the high precision stage is moved in the negative x-axis direction. This orientation angle is defined as the included angle κ and it is controlled by the movement of the x and y axes of the PZT that holds the AFM probe, which is set before machining. In this case, given that the tip path is not parallel to the y axis, as shown in Fig. 6(b), the feed Δ is the distance between two successive and parallel paths:

$$\Delta = \cos\kappa \cdot \frac{V_{stage}}{s} \qquad (2)$$

where V_{stage} is the velocity of the high precision stage and s is the number of cutting lines generated by the reciprocating motion of the tip.

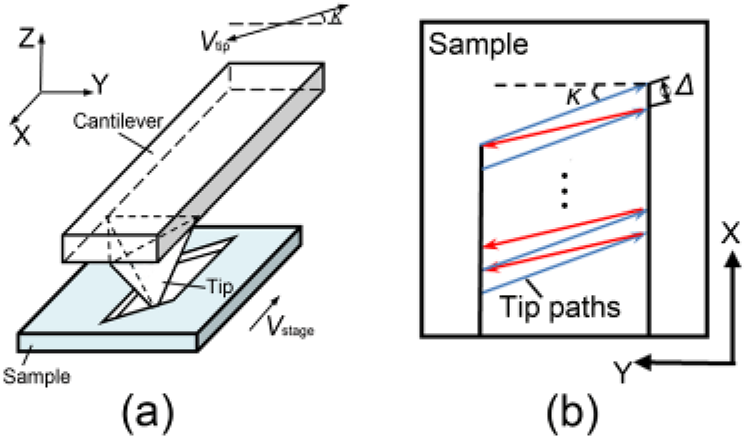

Fig. 6. (a) Schematic diagram of the nanomachining setup with an included angle and (b) the top view of the machining process.

To ensure consistency of the feed value for each machining trial, the velocity of the high precision stage must be adjusted according to the selected value of the included angle. In this study, six included angles were chosen in 10°-increments in the range from 10° to 60°. Fig. 7 shows SEM images of the obtained nanochannels after machining for the six included angles using a feed of 120 nm and a set normal load of 67 µN. For each trial, the distance of the tip reciprocating motion was 20 µm and the travel velocity of the tip was 80 µm/s. Fig. 8 shows higher magnification SEM images of chips formed with included angles of 20°, 30°, and 40°. Fig. 9 shows AFM images of the topography of machined nanochannels with included angles of 10°, 20°, 30°, and 40° after cleaning in ultrasonic solution.

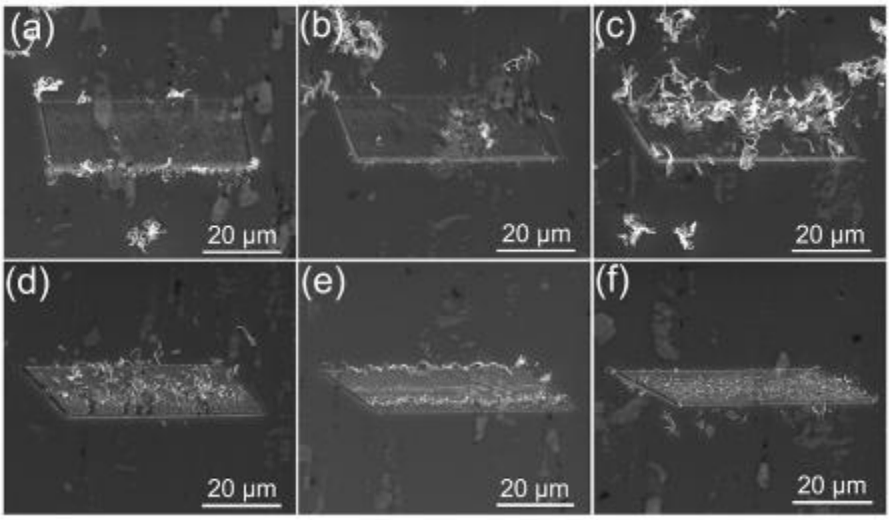

Fig. 7. SEM images of nanochannels machined with included angles of (a) 10°, (b) 20°, (c) 30°, (d) 40°, (e) 50°, and (f) 60°.

For included angles of 10° (Fig. 7(a)) and 20° (Fig. 7(b)), continuous chips formed during machining with almost no residual chips remaining on both sides of the nanochannels, similar to the results obtained for the pure edge-forward condition. Relatively high-quality nanochannels were obtained in both cases, as shown in Fig. 9(a) and (b), and the machined depths of the fabricated nanochannels were approximately 270 and 370 nm, respectively. These values were obtained by averaging three depths measurements taken at three different locations along the machined nanochannel. Both of these depth values are larger than the depth achieved using the pure edge-forward direction.

As shown in Fig. 8(a), the chips formed with the included angle of 20° have a similar morphology to that shown in Fig. 4(d) for the edge-forward direction. Sawtooth structures are also present on one face of the chips because of the mixture of plowing and cutting mechanisms. In addition, the widths of the chips are larger than those shown in Fig. 4(d) because of the larger machined depth. In contrast, large continuous chips formed and accumulated on one side of the channel when machining with an included angle of 30° (Fig. 7(c)). Compared with the chips shown in Fig. 8(a), both the width and the length of the chips formed with this included angle are larger and both sides of the chips are smoother (see Fig. 8(b)). The results for this configuration indicate that cutting with chip formation occurs when the tip moves along the negative *y*-axis direction, as shown in Fig. 6(b), whereas plowing may be the main mechanism during the return path of the tip when completing a full reciprocating motion. The existence of these different mechanisms can be explained by the attack angle along the scratching direction (58°) producing long and smooth chips and the clearance angle being about 32°. In this case, the attack angle is sufficiently large to form continuous chips and the clearance angle does not affect the cutting state. The corresponding depth of the nanochannel is ~520 nm, which is much larger than the depths achieved with included angle from 0° to 20°. Further, owing to the long and continuous chips, the contact area between the tip and chips at the end of the tip travelling trace in one reciprocating cycle would be large. This would lead to a smaller machined depth and skewness of the channel, as shown in the horizontal cross-section in Fig. 9(c). Thus, the cutting angles and chip formation process have a large influence on the depth and quality of the machined nanochannels. In the next section, a scratch model is developed to help explain the effect of the cutting angle on the achieved machined depth.

From Fig. 7(d)–(f), when operating at included angles of ≥40°, intermittent chips are observed together with large burrs on the bottom of the nanochannels. As shown in Fig. 8(c), an included angle of 40° leads to formation of chips that cannot be cut off from the bottom of the channels, resulting in poor surface quality. Moreover, from the AFM image of the nanochannel produced in this case (Fig. 9(d)), the depth is difficult to determine and the bottom surface is relatively rough. These phenomena can be explained as follows. For included angles ≥40°, although the attack angles in the negative *y*-axis direction are all greater than 63°, as shown in Fig. 6(b), the clearance angles and the attack angles in the reciprocating path are all less than 27°. This can result in ineffective removal of material and no chip formation during the scratching process. These conditions are similar to the cutting state illustrated in Fig. 2(c) for the sideface-forward direction. However, the clearance angles in the negative *y*-axis direction and the attack angles in the return path are less than those of the sideface-forward direction. This can cause large surface friction between the flank surface of the tip and the processed material surface, and thus poor surface quality. In summary, 30° is the maximum included angle that should be considered to enable chip formation and effective removal of material along with a high-quality surface.

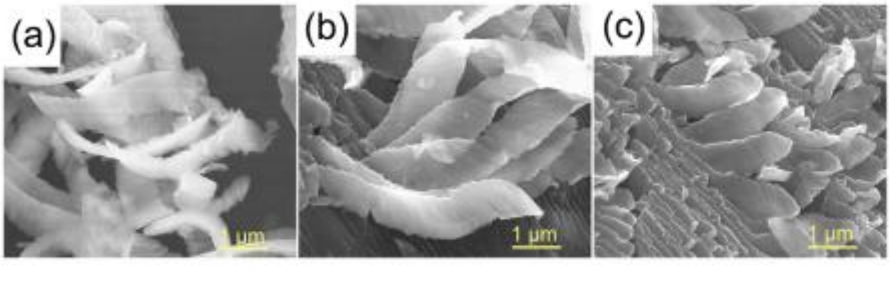

Fig. 8. Local SEM images of the chips formed with included angles of (a) 20°, (b) 30°, and (c) 40°.

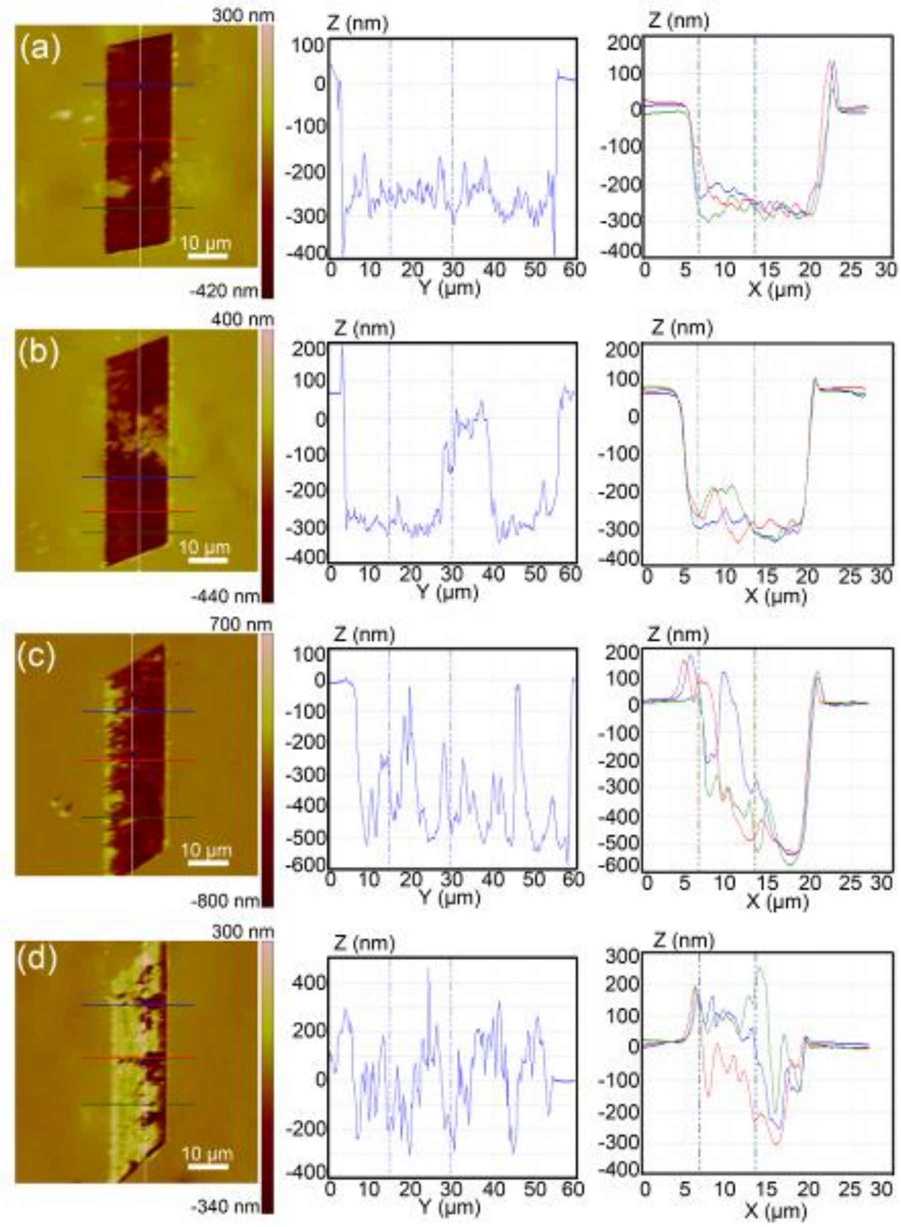

Fig. 9 AFM images of nanochannels machined with included angles of (a) 10°, (b) 20°, (c) 30°, and (d) 40°.

3.3 Modeling the cutting process for the edge-forward configuration with different included angles

In traditional machining, the cutting angle and cutting force are important parameters that govern the process. In particular, the cutting angle has a large influence on chip formation and the resulting cutting force during machining. Typically, using the AFM-based nanomachining method, the normal load applied on the sample is controlled to fabricate nanostructures at the micro/nanoscale. Moreover, the cutting tool used with AFM-based nanomachining is often a three-sided pyramidal tip. Only a few researchers have investigated the cutting angles and cutting forces when machining with an AFM probe, although these factors are very important to understand the material removal mechanisms occurring during the process. Thus, in this section, these parameters are investigated in detail when machining with an AFM tip.

Considering the three-sided pyramidal shape of the diamond tip and the fact that the tip performs reciprocating motion at an included angle with respect to the *y* axis, as shown in Fig. 6, the oblique cutting operation is suitable to represent the cutting operations in this study [31]. Fig. 10(a) shows the side view of the nanomachining process in the edge-forward configuration and Fig. 10(b) shows a schematic diagram of the AFM tip-based oblique cutting process.

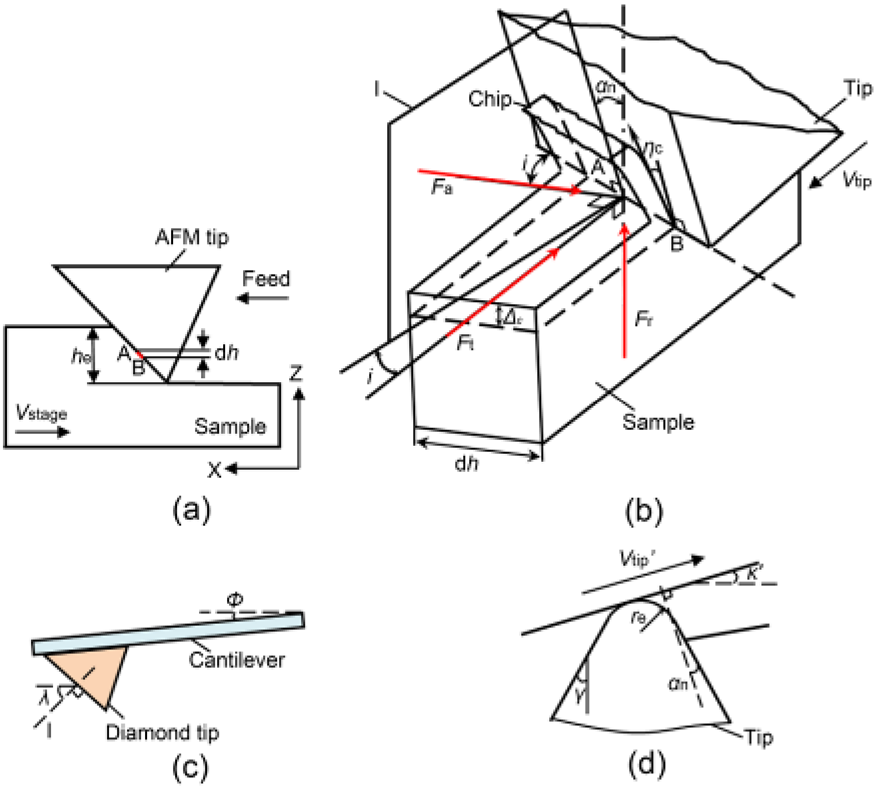

Fig. 10. Schematic diagrams of the (a) side view of the nanomachining process, (b) corresponding detailed representation of the AFM tip-based oblique cutting process, (c) tip mounted angle, (d) local cross-section of the tip during cutting in plane I.

Material removal occurs via the interference between the tip profile and the sample profile along the velocity direction of the tip (V_{tip}). Because the height of the hemispherical top of the tip is calculated to be 25 nm, which is much smaller than the machined depths obtained in this study, the effect of this hemispherical part of the tip is assumed to be negligible. Points A and B in Fig. 10(a) and (b) represent the intersection between the tip and the sample, and they are also the extreme points of the active cutting edge for an infinitesimal cutting depth (dh). Plane I in Fig. 10(b) is the normal plane perpendicular to the cutting edge (vector AB). When V_{tip} is not perpendicular to the cutting edge AB, and hence inclined to the normal plane I by an acute angle, the cutting process can be considered to be an oblique cutting process. The tool inclination angle i can be defined as the acute angle between V_{tip} and plane I. In addition, Φ is the mounted angle of the AFM probe on the AFM head, as shown in Fig. 10(c), which is 12° in this study. Thus, considering the geometrical shape of the diamond tip and this mounted angle, the normal plane I has an acute angle of $\lambda = 67°$ inclined to the horizontal plane. κ is the angle previously defined and shown in Fig. 6. The tool inclination angle i can be determined by

$$\sin i = \sin\kappa \cdot \sin\lambda \tag{3}$$

Fig. 10(d) shows the local cross-section of the tip in plane I. In this plane, κ', which is the corresponding angle of κ, can be obtained by

$$\cos\kappa' = \frac{\cos\kappa}{\cos i} \tag{4}$$

which is the variation angle of the projection of the velocity of the tip (V_{tip}') in plane I. γ is the semi-angle of the cutting tool. The normal rake angle α_{n} can be expressed as

$$\alpha_n = \arccos\kappa' - \gamma \tag{5}$$

r_{e} is the edge radius of the diamond tip, which is 40 nm according to the AFM probe manufacturer.

As shown in Fig. 10(b), the force components F_{t} and F_{r} in oblique cutting are along V_{tip} and normal to V_{tip} in plane I, respectively, while the third force component F_{a} is mutually perpendicular to F_{t} and F_{r}. The three incremental force components, namely, tangential dF_{t}, radial dF_{r}, and axial dF_{a}, acting on depth element (dh) can be expressed as [32]

$$dF_t = (K_{tc}\Delta + K_{te})dh \tag{6a}$$

$$dF_r = (K_{rc}\Delta + K_{re})dh \tag{6b}$$

$$dF_a = (K_{ac}\Delta + K_{ae})dh \tag{6c}$$

where K_{tc}, K_{rc}, and K_{ac} are the cutting force coefficients in the tangential, radial, and axial direction, respectively, and K_{te}, K_{re}, and K_{ae} are the corresponding edge force coefficients. The cutting force coefficients are estimated from the oblique cutting model proposed by Armarego and Brown [32]:

$$K_{tc} = [(\frac{\tau}{\sin(\varphi_n)})(\frac{\cos(\beta_n - \alpha_n) + \tan(i)\tan(\eta_c)\sin(\beta_n)}{\sqrt{\cos^2(\varphi_n + \beta_n - \alpha_n) + \tan^2(\eta_c)\sin^2(\beta_n)}})] \tag{7a}$$

$$K_{rc} = [(\frac{\tau}{\sin(\varphi_n)\cos(i)})(\frac{\sin(\beta_n - \alpha_n)}{\sqrt{\cos^2(\varphi_n + \beta_n - \alpha_n) + \tan^2(\eta_c)\sin^2(\beta_n)}})] \tag{7b}$$

$$K_{ac} = [(\frac{\tau}{\sin(\varphi_n)})(\frac{\cos(\beta_n - \alpha_n)\tan(i) - \tan(\eta_c)\sin(\beta_n)}{\sqrt{\cos^2(\varphi_n + \beta_n - \alpha_n) + \tan^2(\eta_c)\sin^2(\beta_n)}})] \tag{7c}$$

where τ is the shear stress in the shear plane, φ_{n} is the normal shear angle, β_{n} is the normal friction angle, i is the tool inclination, and η_{c} is the chip-flow angle in the rake face. Using the approximate Stabler chip flow rule [33], η_{c} is considered to be equal to i in the present study.

When the size of the uncut chip thickness (Δ_{c}) and the edge radius of the cutting tool (r_{e}) are on a similar size scale, the normal rake angle α_{n} is usually replaced by the effective rake angle α_{t} [34]:

$$\alpha_t = \begin{cases} \arcsin(\frac{\Delta_c}{r_e} - 1); \text{when } \Delta_c < r_e(1+\sin\alpha_n) \\ \alpha_n; \text{when } \Delta_c \ge r_e(1+\sin\alpha_n) \end{cases} \tag{8}$$

According to Budak and Ozlu [35], the normal friction angle β_{n} can be obtained by

$$\tan\beta_n = \tan\beta\cos(\eta_c) \tag{9}$$

where β is the friction angle, which is related to the apparent friction coefficient. The friction angle β is estimated from the following relations [36]:

$$\tan\beta = \frac{\tau_1}{p_0}(1+\rho(1-(\frac{\tau_1}{p_0\mu})^{\frac{1}{\rho}})) \tag{10}$$

$$\frac{\tau_1}{p_0} = \frac{\rho+2}{4(\rho+1)}\frac{\sin(2(\varphi_n+\beta_n-\alpha_n))}{\cos^2(\beta_n)\cos(\eta_c)} \tag{11}$$

where τ_1 is the shear yield strength of the sample material along the so-called sticking region (see Ref. [36]), which corresponds to a region close to the cutting edge at the exit of the shear zone, and p_0 is the normal pressure acting on the tip. ρ is the distribution exponent, and $\rho = 3$ based on an experimental study [37]. μ is the sliding coefficient of friction, which can be obtained by performing a tip sliding test [36]. In this study, to perform this test, a relatively light normal load of 7.9 μN was applied on the surface of the sample by the diamond tip while sliding over the surface. A silicon tip was then used to scan the test region to ensure that there was no groove on the surface of the sample, ensuring that the test was conducted without inducing plastic deformation. The friction force during the test can be determined by

$$f = \alpha \cdot V_f \tag{12}$$

where α is the conversion factor between the lateral voltage signal of the photodetector of the AFM (V_f) and the friction force (f). α can be determined using the method proposed by Varenberg et al., in which the tip is made to slide on a wedge-shaped silicon calibration grating [38]. In this way, α was estimated to be 52.2 μN/V. V_f could then be recorded from the output voltage signal of the PSD in the lateral direction during the sliding test on the aluminum sample. The obtained friction force was 4.2 μN and the sliding coefficient of friction was determined to be 0.53.

To estimate the normal shear angle φ_n, we used the method proposed by Merchant [39]:

$$\varphi_n = \frac{\pi}{4} - \frac{\beta_n}{2} + \frac{\alpha_n}{2} \tag{13}$$

which relies on the assumption that the direction of shear coincides with the direction of maximum shearing stress for a perfectly plastic material.

In the present study, the analytical model proposed by Abdelmoneim and Scrutton [40] was used to estimate the edge force coefficients K_{te}, K_{re}, and K_{ae}:

$$K_{te} = r_e \tau \left(\frac{2\theta_0}{\cos(\theta_0)} + \pi \sin(\theta_0) \tan(\theta_0)\right) \tag{14a}$$

$$K_{re} = r_e \tau (2\sqrt{3} \sin(\theta_0)) \tag{14b}$$

$$K_{ae} = K_{te} \sin(i) \tag{14c}$$

where θ_0 is the neutral point angle, which is considered as 14° in this study [40]. This model was developed for machining where the edge radius and the depth of cut have a similar size scale, and it takes into account rubbing forces because of the plowing state.

When the included angles (κ) of the scratching tests are given, the cutting angles i, α_n, β_n, and φ_n during machining can be obtained by Eqs. (3), (5), (9), and (13), respectively. The calculated results for these angles for each κ when the tip moves along the negative y axis are given in Table 1.

Table 1. Cutting angles in the AFM-based nanomachining process.

κ	i	λ	α_n	β_n	φ_n
0.0°	0.0°	67.0°	−45.0°	17.5°	13.7°
10.0°	9.2°	67.0°	−41.0°	18.2°	15.4°
20.0°	18.4°	67.0°	−36.9°	17.9°	17.6°
30.0°	27.4°	67.0°	−32.3°	16.3°	20.7°
40.0°	36.3°	67.0°	−26.8°	13.7°	24.8°
50.0°	44.8°	67.0°	−20.0°	10.2°	29.9°
60.0°	52.9°	67.0°	−10.9°	6.6°	36.2°

From Table 1, the absolute value of the negative rake angle decreases and the normal shear angle increases with increasing included angle. Chips form more easily and removal of the material is more effective with a relatively small absolute value of the negative rake angle and a relatively large normal shear angle [41]. However, the corresponding clearance angle also decreases with decreasing absolute value of the negative rake angle. In traditional machining, with a small clearance angle, the machined surface can be damaged by the flank face of the cutting tool, which can affect the following cutting path. Moreover, in the return scratching pass, the absolute value of the negative rake angle increases with augmentation of the included angle. With a large absolute value of the negative rake angle, the tip rubs on the surface of the sample, resulting in plowing and ineffective removal of the material (see Fig. 7(d), (e), and (f)). Thus, the included angle has an ideal value to guarantee the machining quality of nanochannels, which is determined to be 30° from the obtained experimental results. To estimate the cutting forces in this chosen range of the included angle, the cutting force coefficients and the corresponding edge force coefficients should first be calculated using Eqs. (7) and (14), and the results are shown in Table 2. Subsequently, the tangential (F_t), radial (F_r), and axial (F_a) cutting forces can be obtained.

Table 2. Cutting force coefficients and the corresponding edge force coefficients

κ	K_{tc}/τ	K_{rc}/τ	K_{ac}/τ	$K_{te}/(\tau\, r_e)$	$K_{re}/(\tau\, r_e)$	$K_{ae}/(\tau\, r_e)$
0.0°	8.19	15.75	0.00	0.44	0.84	0.00
10.0°	7.26	12.18	0.44	0.44	0.84	0.13
20.0°	6.32	8.90	0.92	0.44	0.84	0.27
30.0°	5.45	6.25	1.46	0.44	0.84	0.39

To provide a more intuitive analysis, the tangential, radial, and axial cutting forces for the cutting points dF_t, dF_r, and dF_a can be resolved into the feed force (F_x), friction force (F_y), and normal load (F_z or F_N) acting on the tip in the *X*, *Y*, and *Z* direction, as shown in Fig. 6(a). These forces can be expressed as

$$F_\mathrm{x} = (F_\mathrm{t}\cos i - F_\mathrm{a}\sin i)\cdot\sin\kappa'\cdot\cos\lambda + F_\mathrm{r}\cos\kappa'\cdot\cos\lambda - (F_\mathrm{a}\cos i - F_\mathrm{t}\sin i)\cdot\sin\lambda \quad (15a)$$

$$F_\mathrm{y} = (F_\mathrm{t}\cos i - F_\mathrm{a}\sin i)\cdot\cos\kappa - F_\mathrm{r}\sin\kappa' \quad (15b)$$

$$F_\mathrm{z} = (F_\mathrm{t}\cos i - F_\mathrm{a}\sin i)\cdot\sin\kappa'\cdot\sin\lambda + F_\mathrm{r}\cos\kappa'\cdot\sin\lambda - (F_\mathrm{a}\cos i - F_\mathrm{t}\sin i)\cdot\cos\lambda \quad (15c)$$

For AFM-based nanomachining, the machined depths of the nanochannels can be directly controlled by the applied normal load [16]. In this study, only the normal load in the *Z* direction (F_N) was used to explain the phenomenon that the depth increases with augmentation of the included angle. Moreover, deformation of the cantilever may introduce a difference between the set normal load and the actual normal load because of the lateral force acting on the tip during machining. In our previous study [26], we found that the influence of deformation of the cantilever of the probe was very small when using a diamond tip mounted on a cantilever with large torsional rigidity. Thus, in this study, the normal load applied on the sample is assumed to be constant for different values of the included angle. Given that the cut trajectory of the tip is triangular over a complete reciprocating motion, the uncut chip thickness and the feed are not constant in the cutting direction during the machining process. The average feed value is chosen as half of the set feed for the calculations. In addition, the radius of the tip apex is larger than the radius of the tip edge, which may introduce errors into calculations of the cutting forces using Eq. (15). However, the machined depth is much larger than the height of the tip spherical apex. Therefore, the calculation error because of this can be ignored.

To further investigate the effect of the cutting angle on the machined depth, the four included angles 0°, 10°, 20°, and 30° and two feed values 60 nm and 120 nm were chosen. The normal load used in the scratching tests was 67 μN and the length of the channel was 50 μm. The displacement of tip reciprocating motion was 20 μm. For each nanochannel, three depths at three different locations were averaged to represent the machined depth value. The experimental depths (h_e) obtained for each case are given in Table 3. In the theoretical model, the shear stress is considered to be the same with different machined depths for simplicity. However, in reality, the hardness of the aluminum alloy decreases with augmentation of tip engagement into the surface of the substrate because of the influences of the surface oxide layer and residual stress resulting from the turning process used to prepare the sample. In our previous study [16], the hardness of the 2A12 aluminum alloy sample was determined with nanoindentation equipment. Tabor [42] proposed that the hardness of a metal is three times the value of its yield pressure (σ). Moreover, the shear stress $\tau = \sigma/3$, which is a more accurate estimate accounting for the Taylor factor for crystalline materials [43]. Thus, in this study, the relationship between the shear stress and the hardness of the sample is assumed to be linear. To more intuitively investigate the influence of the cutting angle on the machined depth, the influence of the shear stress variation for different machined depths should be removed from the analysis. In this study, the depths of machined channels with different included angles are compared with the channel with 0° included angle ($h_e(0°)$). Thus, the coefficient of the shear stress $f(\tau)$ is used to separate the shear stress factor, which is obtained by the experimental data reported in Ref. [16]. The experimental ratio of $h_e/h_e(0°)$ without considering the shear stress factor can be obtained by $h_e f(\tau)/h_e(0°)$, and the results are shown in Table 3. Using Eqs. (6) and (15c), the cutting force coefficients, and the corresponding edge force coefficients shown in Table 2, the ratio of the theoretical depth of h_t to $h_t(0°)$ can be calculated, and the results are shown in the Table 3. The experimental values are slightly less than the theoretical data. With augmentation of the included angle, the difference between the theoretical and experimental results becomes larger. A possible reason for this is that the theoretical ratio is calculated along the chip formation direction, whereas in the return direction the absolute value of the negative rake angle becomes larger, which results in a relatively shallow depth. This can affect the contact area between the tip and the sample during the next path along the cutting direction. With augmentation of the included angle, the influence of the return path becomes larger. Moreover, the accuracy of the shear stress estimation used in the theoretical model may contribute to this discrepancy. However, because the experimental values are generally close to the theoretical data, it can be concluded that the developed model is very accurate. Notably, the cutting angles in the AFM-based machining setup also have a substantial influence on chip formation and the quality of nanochannels.

Table 3. Experimental and theoretical machined depth ratios.

κ	Δ (nm)	h_e (nm)	$f(\tau)$	$h_e f(\tau)/h_e(0°)$	$h_t/h_t(0°)$
0.0°	60	402	1.00	1.00	1.00
10.0°	60	519	0.93	1.22	1.24
20.0°	60	623	0.87	1.44	1.63
30.0°	60	851	0.82	1.90	2.18
0.0°	120	208	1	1.00	1.00
10.0°	120	270	0.96	1.19	1.25
20.0°	120	370	0.93	1.53	1.64
30.0°	120	520	0.90	2.03	2.29

4. Conclusions

In this study, nanochannels were machined in an aluminum alloy with a three-sided pyramidal AFM diamond tip, and the feed directions influencing the quality of the machined channels were investigated by experimental and theoretical approaches. First, the influence of three feed directions on the chip formation process and the quality of the machined nanochannels was investigated by analysis of SEM and AFM images. To reveal the machining mechanism, scratching was performed using several feed directions with different included angles and the edge-forward configuration. Finally, an AFM-based cutting model for scratching with the three-sided pyramidal probe in different directions was proposed, and the ratios of the theoretical machined depths were compared with experimental values. Based on the obtained results, the following conclusions can be drawn:

(1) Machining along the edge-forward direction leads to better quality channels, continuous chips, and higher material removal efficiency than scratching in the face- and sideface-forward directions. The face- and sideface-forward directions resulted in poor-quality machined channels and a significant amount of burrs on the bottom of the channels. In addition, when scratching in these directions, the channels had almost no or a much smaller machined depth. This may be because of the plowing mechanism during scratching, which reduces the material removal efficiency.

(2) Continuous chips and high-quality machined nanochannels were obtained when scratching with included angles in the range 0°–30° for the edge-forward direction. In contrast, machining with included angles greater than 30° led to generation of burrs on the bottom of the channels and small machined depths. This may be because of the small clearance angle in the cutting direction and the large absolute value of the negative rake angle in the return direction. A small clearance angle in the cutting direction can result in the machined material interacting with the flank

surface of the probe, and a large absolute value of the negative rake angle in the return direction can cause the machining state to be dominated by plowing.

(3) Using a theoretical model, the increase of the machined depth with increasing included angle in the range 0°–30° could be explained. Further, the cutting angle plays an important role in the nanomachining process, which can affect chip formation, machining quality, and material removal efficiency.

Acknowledgments

The authors gratefully acknowledge financial supports of Foundation for National Natural Science Foundation of China (51222504, 21327002), the Author of National Excellent Doctoral Dissertation of PR China (201031), the Program for New Century Excellent Talents in University (NCET-11-0812) and the National Program for Support of Top-notch Young Professors.

References

[1] K. B. Sung, K. P. Liao, Y. L. Liu, et al., Development of a nanofluidic preconcentrator with precise sample positioning and multi-channel preconcentration, Microfluid Nanofluid 14 (2013) 645-655.

[2] J. M. Perry, K. Zhou, Z. D. Harms, et al., Ion Transport in Nanofluidic Funnels, ACS Nano 4 (7) (2010) 3897-3902.

[3] R, A, Barton, B. Ilic, S. S. Verbridge, et al., Fabrication of a Nanomechanical Mass Sensor Containing a Nanofluidic Channel, Nano Letters 10 (2010) 2058-2063.

[4] S. J. Kim, L. D. Li, J. Han, Amplified Electrokinetic Response by Concentration Polarization near Nanofluidic Channel, Langmuir 25 (13) 7759-7765.

[5] N. Yanai, T. Uemura, S. Horike, et al., Inclusion and dynamics of a polymer-Li salt complex in coordination nanochannels, Chemical Communications 47 (2011) 1722-1724.

[6] R. Chantiwas, S. Park, S. A. Soper et al., Flexible fabrication and applications of polymer nanochannels and nanoslits, Chemical Society Reviews 40 (2011) 3677-3702.

[7] R. Garcia, A. W. Knoll, E. Riedo, Advanced scanning probe lithography, Nature Nanotechnology 9 (2014) 577-587.

[8] L. D. Menard, J. M. Ramsey, Fabrication of Sub-5 nm Nanochannels in Insulating Substrates Using Focused Ion Beam Milling, Nano Letters 11 (2) (2011) 512-517.

[9] Y. Liao, J. X. Song, E. Li, et al., Rapid prototyping of three-dimensional microfluidic mixers in glass by femtosecond laser direct writing, Lab on a Chip 12 (2012) 746-749.

[10] N. R. Devlin, D. K. Brown, P. A. Kohl, Patterning decomposable polynorbornene with electron beam lithography to create nanochannels, Journal of Vacuum Science and Technology B 27 (2009) 2508.

[11] A. A. Tseng, Advancements and challenges in development of atomic force microscopy for nanofabrication, Nano Today 6 (2011) 493-509.

[12] Y. D. Yan, T. Sun, Y. C. Liang, et al., Investigation on AFM-based micro/nano-CNC machining system, International Journal of Machine Tools and

Manufacture 47 (2007) 1651-1659.

[13] M. Malekian, S. S. Park, D. Strathearn, et al., Atomic force microscope probe-based nanometric scribing, Journal of Micromechanics Microengineering 20 (2010) 115016.

[14] Z. Kato, M. Sakairi, H. Takahashi, Nanopatterning on aluminum surfaces with AFM probe, Surface and Coatings Technology 169-170 (2003) 195-198.

[15] E. B. Brousseau, B. Arnal, S. Thiery, et al., Towards CNC Automation in AFM Probe-Based Nano Machining, International Conference on Micromanufacture, Victoria, Canada, 2013 P. 95.

[16] Y. Q. Geng, Y. D. Yan, Y. M. Xing, et al., Modelling and experimental study of machined depth in AFM-based milling of nanochannels, International Journal of Machine Tools and Manufacture 73 (2013) 87-96.

[17] Y. D. Yan, Z. J. Hu, X. S. Zhao, et al., Top-Down Nanomechanical Machining of Three-Dimensional Nanostructures by Atomic Force Microscopy, Small 6 (6) (2010) 724-728.

[18] I. H. Sung, D. E. Kim, Nano-scale patterning by mechano-chemical scanning probe lithography, Applied Surface Science 239 (2005) 209-221.

[19] X. S. Zhao, Y. Q. Geng, W. B. Li, et al., Fabrication and measurement of nanostructures on the micro ball surface using a modified atomic force microscope, Review of Scientific Instruments 83 (2012) 115104.

[20] A. A. Tseng, S. Jou, J. C. Hang, et al., Scratch properties of nickel thin films using atomic force microscopy, Journal of Vacuum Science Technology B 28 (2010)

202-210.

[21] Z. X. Dong, U. C. Wejinya, Atomic force microscopy based repeatable surface nanomachining for nanochannels on silicon substrates, Applied Surface Science 258 (22) 2012 8689-8695.

[22] Z. Q. Wang, S. Tung, Z. L. Dong, Material removal model for AFM-based nanochannel fabrication, Wear 278-279 (2012) 71-76.

[23] Y. Q. Geng, Y. D. Yan, B. W. Yu, et al., Depth prediction model of nano-grooves fabricated by AFM-based multi-passes scratching method, Applied Surface Science 313 (2014) 615-623.

[24] Z. C. Lin, Y. C. Hsu, A calculating method for the fewest cutting passes on sapphire substrate at a certain depth using specific down force energy with an AFM probe, Journal of Materials Processing Technology 212 (11) 2321-2331.

[25] Y. Q. Geng, Y. D. Yan, X. S. Zhao, et al., Fabrication of millimeter scale nanochannels using the AFM tip-based nanomachining method, Applied Surface Science 266 (2013) 386-394.

[26] Y. Q. Geng, Y. D. Yan, Y. M. Xing, et al., Effect of cantilever deformation and tip-sample contact area on AFM nanoscratching, Journal of Vacuum Science and Technology B 31 (6) (2013) 061802.

[27] L. S. Dongmo, J. S. Villarrubia, S. N. Jones, et al., Experimental test of blind tip reconstruction for scanning probe microscopy, Ultramicroscopy 85 (2000) 141-153.

[28] K. Hokkirigawa, K. Kato, An experimental and theoretical investigation of plowing, cutting and wedge formation during abrasive wear, Tribology International

21 (1988) 51-57.

[29] V. N. Koinkar, B. Bhushan, Scanning and transmission electron microscopies of single-crystal silicon microworn/machined using atomic force microscopy, Journal of Material Research 12 (12) (1997) 3219-3224.

[30] Y. C. Zhang, T. Mabrouki, D. Nelias, et al., Chip formation in orthogonal cutting considering interface limiting shear stress and damage evolution based on fracture energy approach, Finite Elements in Analysis and Design 47 (2011) 850-863.

[31] E. J. A. Armarego, A generic mechanics of cutting approach to predictive technology performance modeling of the wide spectrum of machining operations, Machining Science and Technology: An International Journal 2 (2) (1998) 191-211.

[32] E. J. A. Armarego, R. H. Brown, The Machining of Metals, Prentice-Hall, Englewood Cliffs, New Jersey, 1969.

[33] G. V. Stabler, The fundamental geometry of cutting tools, Proceeding of the Institution of Mechanical Engineers 165 (1951) 14-26.

[34] S. Venkatachalam, X. Li, S. Y. Liang, Predictive modeling of transition undeformed chip thichness in ductile-regime micro-machining of single crystal brittle materials, Journal of Materials Processing Technology 209 (2009) 3306-3319.

[35] E. Budak, E. Ozlu, Development of a thermomechanical cutting process model for machining process simulations, CIRP Annals-Manufacturing Technology 57 (1) (2008) 97-100.

[36] E. Ozlu, E. Budak, A. Molinari, Analytical and experimental investigation of rake contact and frication behavior in metal cutting, International Journal of Machine Tools

and Manufacture 49 (2009) 865-875.

[37] E. Ozlu, E. Budak, A. Molinari, Thermomechanical Modeling of Orthogonal Cutting Including the Effect of Stick-Slide Regions on the Rake Face, 10th CIRP International Workshop on Modeling of Machining Operations (2007) Calabria, Italy

[38] M. Varenberg, I. Etsion, G. Halperin, An improved wedge calibration method for lateral force in atomic force microscopy, Review of Scientific Instruments 74 (2003) 3362-3367.

[39] M. E. Merchant, Mechanics of the metal cutting process. II. Plasticity conditions in orthogonal cutting, Journal of Applied Physics 16 (1945) 318-324.

[40] M. E. S. Abdelmoneim, R. F. Scrutton, Tool edge roundness and stable build up formation in finish machining, Transaction of the ASME Journal of Engineering and Industrial 96 (1974) 1258-12676.

[41] M. Günay, E. Aslan, İ. Korkut, et al., Investigation of the effect of rake angle on main cutting force, International Journal of Machine Tools and Manufacture 44 (2004) 953-959.

[42] D. Tabor, The Hardness of Metals, Oxford University Press, Oxford, 1951.

[43] Y. V. Srinivasa, M. S. Shunmugam, Mechanistic model for prediction of cutting forces in micro end-milling and experimental comparison, International Journal of Machine Tools and Manufacture 67 (2013) 18-27.

Figure captions

Fig. 1. (a) Schematic diagram of the modified AFM probe-based machining system, (b) image of the diamond probe, and schematic diagrams of (c) side and (d) front views of the diamond tip.

Fig. 2. Schematic diagrams of the three feed directions considered: (a) edge-forward, (b) face-forward, (c) sideface-forward.

Fig. 3. Schematic diagrams of side views of the nanomachining processes: (a) edge-forward, (b) face-forward, and (c) sideface-forward. Schematic diagrams of cross-sectional views of the nanomachining processes: (d) A-A section in Fig. 3(a), (e) B-B section in Fig. 3(b), and (f) C-C section in Fig. 3(c).

Fig. 4. SEM images of machined nanochannels: (a) edge-forward, (b) face-forward, and (c) sideface-forward. Magnified SEM images of chips or burrs: (d) edge-forward, (e) face-forward, and (f) sideface-forward.

Fig. 5. AFM images of the machined nanochannels: (a) edge-forward, (b) face-forward, and (c) sideface-forward.

Fig. 6. (a) Schematic diagram of the nanomachining setup with an included angle and

(b) the top view of the machining process.

Fig. 7. SEM images of nanochannels machined with included angles of (a) 10°, (b) 20°, (c) 30°, (d) 40°, (e) 50°, and (f) 60°.

Fig. 8. Local SEM images of the chips formed with included angles of (a) 20°, (b) 30°, and (c) 40°.

Fig. 9 AFM images of nanochannels machined with included angles of (a) 10°, (b) 20°, (c) 30°, and (d) 40°.

Fig. 10. Schematic diagrams of the (a) side view of the nanomachining process, (b) corresponding detailed representation of the AFM tip-based oblique cutting process, (c) tip mounted angle, (d) local cross-section of the tip during cutting in plane I.

Table captions

Table 1. Cutting angles in the AFM-based nanomachining process.

Table 2. Cutting force coefficients and the corresponding edge force coefficients

Table 3. Experimental and theoretical machined depth ratios.